Downloaded via PENNSYLVANIA STATE UNIV on April 27, 2021 at 14:04:18 (UTC). See https://pubs.acs.org/sharingguidelines for options on how to legitimately share published articles.



www.acsnano.org

Photophysics and Electronic Structure of Lateral Graphene/MoS₂ and Metal/MoS₂ Junctions

Shruti Subramanian, Quinn T. Campbell, Simon K. Moser, Jonas Kiemle, Philipp Zimmermann, Paul Seifert, Florian Sigger, Deeksha Sharma, Hala Al-Sadeg, Michael Labella, III, Dacen Waters, Randall M. Feenstra, Roland J. Koch, Chris Jozwiak, Aaron Bostwick, Eli Rotenberg, Ismaila Dabo, Alexander W. Holleitner, Thomas E. Beechem, Ursula Wurstbauer, and Joshua A. Robinson*



Cite This: ACS Nano 2020, 14, 16663-16671



ACCESS

Metrics & More

Article Recommendations

Supporting Information

Article Recommendations

Supporting Information

Article Recommendations

Supporting Information

Ti/Au

Ti/Au

Ti/Au

Ti/Au

Scanning Electron Micrograph

Photocurrent (A)

ABSTRACT: Integration of semiconducting transition metal dichalcogenides (TMDs) into functional optoelectronic circuitries requires an understanding of the charge transfer across the interface between the TMD and the contacting material. Here, we use spatially resolved photocurrent microscopy to demonstrate electronic uniformity at the epitaxial graphene/molybdenum disulfide (EG/MoS₂) interface. A $10 \times$ larger photocurrent is extracted at the EG/MoS₂ interface when compared to the metal (Ti/Au)/MoS₂ interface. This is supported by semi-local density functional theory (DFT), which predicts the Schottky barrier at the EG/MoS₂ interface to be ~2× lower than that at Ti/MoS₂. We provide a direct visualization of a 2D material Schottky barrier through combination of angle-resolved photoemission spectroscopy with spatial resolution selected to be ~300 nm (nano-ARPES) and DFT calculations. A bending of ~500 meV over a length scale of ~2–3 μ m in the valence band maximum of MoS₂ is observed via nano-ARPES. We explicate a correlation between experimental demonstration and theoretical predictions of barriers at graphene/TMD interfaces. Spatially resolved photocurrent mapping allows for directly visualizing the uniformity of built-in electric fields at heterostructure interfaces, providing a guide for microscopic engineering of charge transport across heterointerfaces. This simple probe-based technique also speaks directly to the 2D synthesis community to elucidate electronic uniformity at domain boundaries alongside morphological uniformity over large areas.

KEYWORDS: photocurrent, graphene contacts, heterostructure, ARPES, Schottky barrier, molybdenum disulfide, first-principles calculations

wo-dimensional (2D) van der Waals semiconducting materials, such as transition metal dichalcogenides (TMDs), are of interest because of their strong light—matter interaction dominated by exciton phenomena. Furthermore, van der Waals crystals are a highly tunable and versatile material systems that are poised to impact flexible and transparent electronics, optoelectronics, optoelectronics, spin- and

Received: March 25, 2020
Accepted: November 10, 2020
Published: November 16, 2020





valleytronics, ¹⁰ catalysis, ^{11–13} biomedical ^{14–16} and sensor ^{17,18} applications, and next-generation quantum materials. ^{19–23} Additionally, semiconducting 2D crystals can be engineered by external stimuli such as doping, ^{24,25} strain, ^{26,27} defects, ²⁸ pressure, ²⁹ and environment; ³⁰ by interaction with light; ³¹ or in moiré superlattice structures. ³² Key to the integration of semiconducting TMDs into functional circuitries is understanding the charge transfer across a 2D semiconductor and metallic heterojunction allowing for them to be precisely engineered to the specific functionality. In this regard, lateral junctions between molybdenum disulfide (MoS₂) and conventional metals, as well as MoS₂ and graphene, are utilized in electronic and optoelectronic device schemes with graphene, providing better contact behavior ^{33,34} and tunability due to its semi-metallic behavior. ³⁵

Here, we investigate the local charge-transfer characteristics and the lateral heterogeneity of metal/MoS2 and graphene/ MoS₂ junctions via scanning photocurrent microscopy and elucidate the band bending of both structures by a combination of angle-resolved photoemission spectroscopy with spatial resolution selected to be ~300 nm (nano-ARPES) and DFT calculations. Illustrating the close correlation between experimental demonstrations and theoretical predictions of barriers at graphene/TMD interfaces allows us to develop a comprehensive understanding of charge transfer, aiding the microscopic engineering of charge transport across heterointerfaces. Direct visualization of built-in fields over large areas at heterostructure interfaces via scanning photocurrent microscopy speaks directly to the 2D synthesis community to correlate and demonstrate electronic uniformity alongside morphological uniformity.

RESULTS AND DISCUSSION

Efficient electron-hole pair (e-h+) generation in MoS₂based devices upon photoexcitation is responsible for a singlelayer MoS2-based photodetector exhibiting a photoresponsivity reaching 880 A/W.36 Despite the rich photophysics, the performance of MoS2 devices that rely on efficient photocurrent generation is limited by large exciton binding energies and the resulting excited-state decay. ^{37–40} Slow photoresponse dynamics observed in MoS2-based devices necessitates a comprehensive understanding of photocurrent dynamics and charge carrier recombination in MoS₂. High-performance optoelectronic detectors require efficient separation of charge carriers following photogeneration to prevent them from recombination before being collected at the electrodes. This separation of e-h+ pairs is facilitated by the existence of a built-in electric field in the system, which leads to the idea of constructing an electronic barrier in the system, away from the metal contacts, to aid the separation of charge carriers. In this work, we examine an epitaxial graphene (EG)/MoS₂ lateral heterostructure exhibiting a uniform built-in electric field at the interface while using 2-3 layer EG as the contact material and allowing for an efficient separation of photogenerated charge carriers. EG/MoS₂ lateral heterostructures are synthesized in the same controllable manner as previously demonstrated by Subramanian et al. with the resulting structure having a \sim 50-200 nm overlap of the multilayer MoS2 onto the edge of the patterned EG³³ as shown in the schematic of Figure 1a,b.

Spatial photocurrent mapping reveals the intrinsic photoresponse at the EG/MoS₂ and the metal/MoS₂ interfaces. The built-in electric field and photogenerated carrier extraction are compared utilizing photocurrent mapping of two synthesized

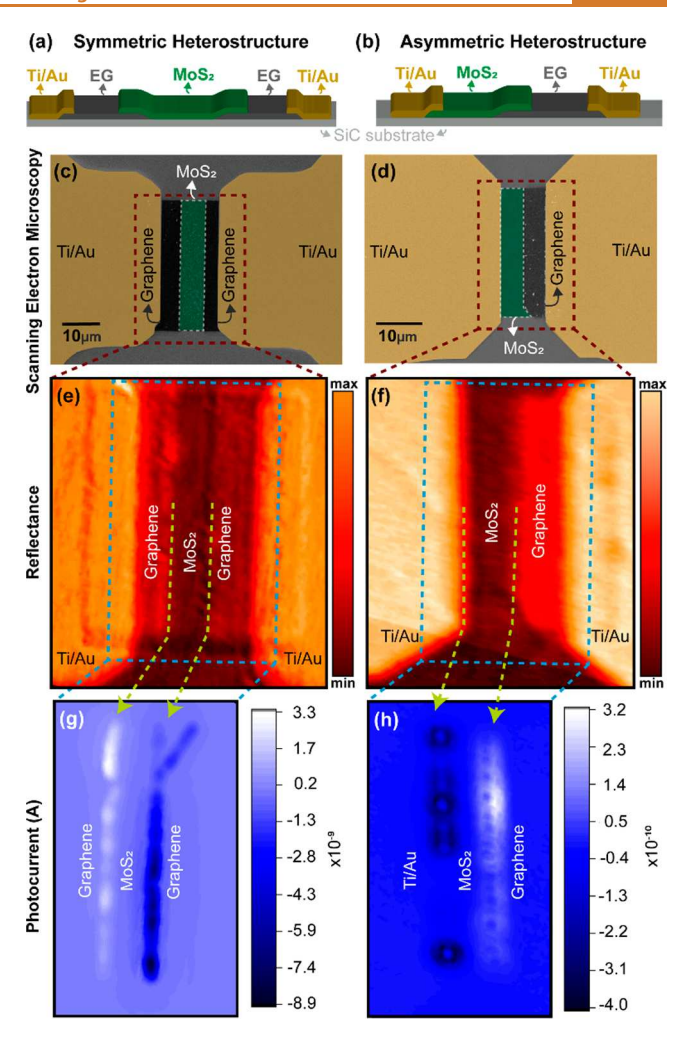


Figure 1. (a) Schematic showing the synthesized symmetric EG/ MoS₂/EG device lateral heterostructure with the overlap of the MoS₂ onto the edge of the patterned EG. (b) Schematic of the asymmetric heterostructure device with metal/MoS₂/EG configuration. (c) False-color scanning electron microscopy (SEM) image of the symmetric heterostructure with EG on both sides of the MoS₂. (d) SEM image of the asymmetric heterostructure with EG on one side and Ti/Au metal on the other. (e) Reflectance map of the symmetric heterostructure zoomed in from panel c. (f) Reflectance map of the asymmetric heterostructure zoomed in from panel d. (\bar{g}) Photocurrent map (at zero applied bias) of the EG/MoS₂/EG heterostructure displaying photoactivity at the EG/ MoS₂ interface. No photoactivity is seen at the metal/EG interface. Dotted lines are drawn to guide the eye to the photoactive interface. (h) Photocurrent map (at zero applied bias) of the metal/MoS₂/EG heterostructure displaying "patchy" photo-activity at the metal/MoS2 interface as compared to the EG/MoS2 interface. 10× reduction in overall photocurrent is observed when compared to panel g.

heterostructure systems (Figure 1): (i) a symmetric lateral heterostructure consisting of metal/EG/MoS₂/EG/metal as shown in Figure 1a,c and (ii) an asymmetric lateral heterostructure consisting of metal/MoS₂/EG/metal as shown in Figure 1b,d. The spatial resolution of photocurrent in 2D heterostructures allows for discerning local variations in the electric field. An optical probe maps the reflection from the two heterostructure systems, as shown in panels e and f of Figure 1 for the symmetric and asymmetric heterostructure systems, respectively, and this is directly coupled with the

photocurrent maps. The different components of the heterostructure devices have different optical contrasts, as seen in the reflectance maps. Photocurrent is observed at the heterostructure interfaces as shown in Figure 1g,h and is attributed to two mechanisms contributing to the photocurrent as extensively studied by Parzinger *et al.*: the primary contributor is the photovoltaic effect, *i.e.*, the generation of e^--h^+ pairs and their subsequent spatial dissociation due to an electric field, and the secondary contributor is the photothermoelectric effect that allows for electrons to have a flux in response to the established temperature gradient by laser irradiation.

The presence of a depletion region at the heterostructure interface leads to a measurable photocurrent upon illumination. For MoS_2 multilayers, if the excitation energy is less than the direct bandgap but more than the indirect bandgap, e^--h^+ pairs will still be generated, but with reduced probability because this transition requires a phonon to change momentum. The lateral heterostructures studied here are dominated by multilayer MoS_2 , especially at the EG/MoS_2 heterostructure interface. We illuminate the heterostructures using the emission line of an Ar/Kr laser at 488 nm (2.54 eV), whose energy is always greater than the direct bandgap of MoS_2 .

The time-integrated photocurrent at heterostructure interfaces is primarily attributed to the photovoltaic effect. 9 Apart from an observation of a measurable photocurrent at the heterostructure interfaces, there are further subtleties visible from the photocurrent maps in Figure 1. Considering Figure 1g, the photo-active interface is the EG/MoS₂ interface, indicating the presence of a Schottky barrier that separates photogenerated charge carriers.⁴⁴ Additionally, the metal/EG interface in the heterostructure system is not photo-active. This is contrary to the observations of photocurrent in exfoliated and CVD graphene at metal contacts where the Schottky barrier is formed. 45-48 Here, the intrinsic polarization of the silicon carbide (SiC) substrate electrostatically dopes EG *n*-type, reducing the Schottky barrier at the metal(Ti/Au)/ EG interface. In contrast, both exfoliated and CVD graphene are typically p-type, ^{49,50} forming a much larger Schottky barrier with the Ti/Au metal stack, thus enabling significant spacecharge regions at the interface. Epitaxial graphene on SiC also exhibits less surface impurities compared to CVD and exfoliated graphene because it does not undergo polymeric transfer processes, which may be a contributing factor to the reduced Schottky barrier at the metal (Ti/Au)/EG interface. All measurements are performed in vacuum to avoid the environmental doping of the 2D materials leading to changes in their Schottky barriers. The photocurrent landscape in the symmetric heterostructure is uniform through the length of the device as compared to the asymmetric heterostructure (see Supporting Information, section S.1). Importantly, a uniform photocurrent exists along the length of the EG/MoS₂ interface regardless of device symmetry (Figure 1g,h), noting the existence of a uniform built-in electric field due to a pristine EG/MoS₂ interface. In contrast, the metal/MoS₂ interface exhibits a non-uniform photocurrent signal (Figure 1h) (photocurrent standard deviation (σ) for the metal/MoS₂ > 1.5× EG/MoS₂; see Supporting Information, section S.1), possibly resulting in current crowding and localized heating of the device. We note that the laser illumination occurs through the contact layer (EG or 20 nm of Ti/Au; 5 nm Ti + 15 nm Au). A non-negligible part of the light, ~25%, is absorbed by

the Ti/Au metal contact stack (calculations done on www. filmetrics.com/reflectance-calculator based on the complexmatrix form of the Fresnel equations). 51-55 This can lead to heating of the metal contact and may provide additional contributions to the observed photocurrent via thermal effects that could have opposite sign and spatial extension across the junction. Together with the reduced dark current, these additional contributions may be responsible for the reduced photocurrent signal in the asymmetric heterostructure when compared to the symmetric heterostructure. The improved uniformity of the built-in field at the EG/MoS₂ interface (Figure 1d) allows for efficient charge separation and an improved electronic conduction through the entire heterostructure system, as evidenced by >10× increase in the measured photocurrent compared to the asymmetric device (see Supporting Information, section S.1). This trend is observed in all tested devices, spanning different samples, and directly corroborates our previous work where EG has been shown to be a better contact to semiconducting MoS₂ compared to conventional metals.³³

Semi-local density functional theory (DFT) predicts the Schottky barrier at the EG/MoS₂ interface to be ~2× lower than that of Ti/MoS₂. Prediction of the Schottky barrier from first-principles necessitates, initially, calculations of work functions (ϕ) of the individual components—pristine graphene ($\phi_{\rm gr}$), MoS₂ ($\phi_{\rm MoS_2}$), and Ti ($\phi_{\rm Ti}$)—and the relaxed heterointerfaces ($\phi_{\rm EG/MoS_2}$ and $\phi_{\rm Ti/MoS_2}$), summarized in Table 1. In this case, however, the work function of epitaxial

Table 1. Work Functions of Both Isolated Materials and Interfaces as Calculated from DFT^a

material	work function (eV)
pristine graphene $(\phi_{ m gr})$	3.92
$ ext{MoS}_2 \ (\phi_{ ext{MoS}_2})$	3.78
SiC (ϕ_{SiC})	4.06
Ti $(\phi_{ ext{Ti}})$	4.02
EG on SiC $(\phi_{ ext{EG}})$	3.99
EG/MoS $_2$ interface ($\phi_{ ext{EG/MoS}_2}$)	3.55
$ ext{Ti/MoS}_2$ interface $(\phi_{ ext{Ti/MoS}_2})$	3.21

"A comparison with alternate DFT functionals is included in Supporting Information, section S.2.

graphene on SiC substrate, termed EG ($\phi_{\rm EG}$), is dominated by the intrinsic polarization in the SiC substrate, necessitating consideration of the SiC work function ($\phi_{\rm SiC}$). Previous first-principles calculations suggest work functions of undoped graphene, MoS₂, and Ti to be 4.23, 4.05, and 4.38 eV, respectively. S6-S8 Here the trend is similar, but the absolute value is consistently lower by ~0.3 eV because of different parameterizations of the exchange-correlation functionals and van der Waals corrections in other works. Because the choice of parameterizations affects the absolute values of the work function but not the relative differences between them, the barrier calculations are considered accurate. $\phi_{\rm gr}$ and $\phi_{\rm SiC}$ differ by ~0.15 eV, leading to an equilibrium $\phi_{\rm EG}$ that is calculated from the SiC/EG interfacial dipole as 3.99 eV.

The total voltage drop $\Delta \phi$ across the junction is defined as $\Delta \phi = \phi_{EG} - \phi_{EG/MoS_2}$, leading to $\Delta \phi = 0.45$ and 0.81 V for EG/MoS₂ and Ti/MoS₂, respectively. To calculate the height of the Schottky barrier (ϕ_B) , we apply a technique developed

for semiconductor interfaces, known to take into account Fermi level pinning ^{60,61} (see Supporting Information, section S.2):

$$\phi_{\rm B} = \frac{\varepsilon \varepsilon_0}{2e_0 N_{\rm d}} \left| \frac{\mathrm{d}\varphi}{\mathrm{d}z} (z_{\rm c}) \right|^2 \tag{1}$$

where φ is the electric potential of the equilibrium interface along the z-axis perpendicular to the plane of the interface, e_0 the electron charge, and $N_{\rm d}$ the three-dimensional defect density in the semiconductor; ε and ε_0 are the dielectric constant of MoS₂ ($\varepsilon=4.3$)⁶² and the vacuum permittivity, respectively. $z_{\rm c}$ is the location along the transverse axis marking the transition between the quantum mechanical region of the interface model and the one-dimensional continuum (Mott-Schottky) description of the bulk semiconductor; $z_{\rm c}$ is located two layers within the semiconductor to fully capture the effects of the interface before transitioning to a bulk model. The only unknown in eq 1 is $N_{\rm d}$. Following the method of Kim et al., ⁶³ we use the density that produces the best fit with the experimental nano-ARPES shown later, $N_{\rm d}=4\times10^{12}$ cm⁻³.

The Schottky barrier of the EG/MoS₂ interface is predicted to be 0.44 eV. This compares favorably with the previous predictions (0.4 eV) for undoped graphene/MoS₂ junction⁶⁴ and reasonably with the prediction of 0.6 eV by Jin et al., using many-body perturbation (G₀W₀) calculations and a single monolayer of both graphene and MoS2.65 A notable feature of the EG/MoS₂ interface in this study is the high fraction of $\Delta \phi$ compensated by the Schottky barrier at the interface. One explanation is that atomically "clean" interfaces, such as the EG/MoS₂, have less covalent and ionic bonds and thus lower surface states, causing a larger fraction of potential offset $\Delta \phi$ to be taken up by the Schottky barrier $\phi_{\rm B}$. In contrast, the Schottky barrier of the Ti/MoS₂ interface is predicted to be 0.79 eV. The voltage drop due to surface states at the interface barrier is ~2× larger for Ti/MoS₂ than for EG/MoS₂, because of increased charge trapping at the interface, indicating a rougher interfacial contact with more ionic and covalent bonds. The ionic and covalent nature of the interfaces was confirmed with Bader analysis (see Supporting Information, section S.2

Temperature-dependent gated current (I-V-T) measurements validate Schottky barrier predictions for EG-contacted MoS₂ and Ti/Au metal contacted MoS₂. Electrostatic double layer (EDL) gating is implemented in a helium-cooled cryostat; the temperature range used is 3-300 K, and the gate voltage (V_g) range used is -2.5 V to +2.5 V. The Arrhenius equation is used to extract the apparent Schottky barrier heights for the two structures (see Supporting Information, section S.3 for further details). EG/MoS₂ heterostructure interface is shown to have a reduced Schottky barrier as compared to Ti/Au contacted MoS₂ in Figure 2e; this result corroborates the photocurrent measurements and the theory calculations of Schottky barrier heights. The difference in the experimental and predicted values is due to the complex interaction of the non-ideal materials with their substrates and dielectric environments. For instance, while we do see significant covalent bonding and intermixing at the Ti/ MoS₂ interface in our calculations, previous literature has found a large interlayer of Ti and MoS2 which is computationally prohibitive to predict.⁶⁶ This may lead to an increase in the predicted Fermi level pinning at this interface and a decrease in the predicted Schottky barrier. Having established

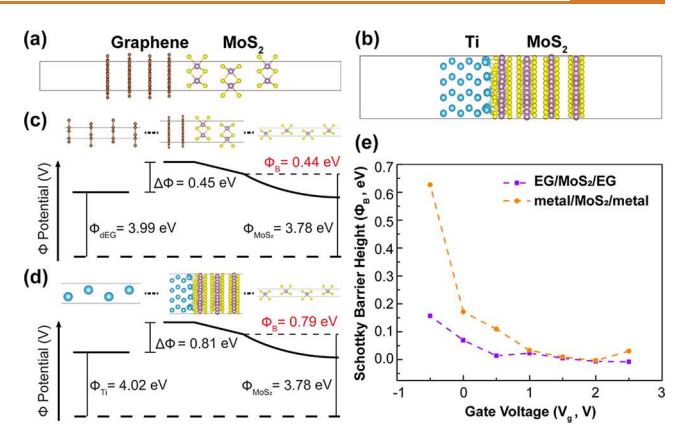


Figure 2. Structures of the (a) EG/MoS_2 interface and (b) Ti/MoS_2 interface from electronic-structure DFT calculations. (c) Diagram of the potential across the EG/MoS_2 heterointerface. The interfacial potential difference $\Delta\phi$ is compensated by a potential drop at the interface (calculated from semi-local DFT) and by a Schottky barrier ϕ_B (calculated using DFT-continuum embedding techniques; see refs 60 and 61). The equilibrium voltage distribution is determined by self-consistently matching the final work functions of the doped graphene and the interface. (d) The same diagram as in panel c, showing a higher value of predicted Schottky barrier at the Ti/MoS_2 interface. (e) Experimental Schottky barriers extracted using Arrhenius plots from temperature-dependent gated current measurements (I-V-T) show a lower value of the Schottky barrier at the EG/MoS_2 interface as compared to the Ti/MoS_2 interface.

that the EG/MoS $_2$ heterointerface is more efficient for charge separation via spatially resolved photocurrent measurements and Schottky barrier extraction, it is essential to understand the specific movement of charge carriers at the EG/MoS $_2$ heterointerface.

Angle-resolved photoemission spectroscopy with selected spatial resolution of ~300 nm (nano-ARPES) visualizes spatial variation in electronic band structures at the EG/MoS₂ heterostructure interface to understand the photo-generated charge transfer. A lower Schottky barrier at the photo-active EG/MoS₂ interface is coupled with a uniform built-in electric field aiding efficient charge separation. The spatial variations in the electronic band structure across the lateral EG/MoS₂/EG interface (as shown in Figure 3a) are investigated at steady state by means of synchrotron-based nano-ARPES. The lateral heterostructure in this experiment is intentionally not allowed to coalesce through the width of the channel between the EG, to enable the study of variations in the electronic structure with edges, where the X-ray probe is focused by a Fresnel zone plate and scanned across the sample. The ARPES band structure I(E, k) is measured at every spatial point coordinate (x, y)creating a 4-dimensional (4D) dataset; E is the binding energy referenced to the Fermi level, k the in-plane momentum along the orientation of the analyzer entrance slit, and I the intensity of the obtained signal (see Supporting Information, section S.4 for the schematic of the nano-ARPES setup). In this scanning mode, nano-ARPES is particularly suited for flat conductive samples, providing a well-defined surface normal and thus a well-preserved momentum resolution. Room-temperature nano-ARPES results obtained with 98 eV photons and an Xray spot size of ~300 nm FWHM across the MoS₂ channel are summarized in Figure 3.

The valence band maximum in MoS_2 bends ~500 meV over a length scale of 2–3 μ m from the edge of the EG/MoS₂

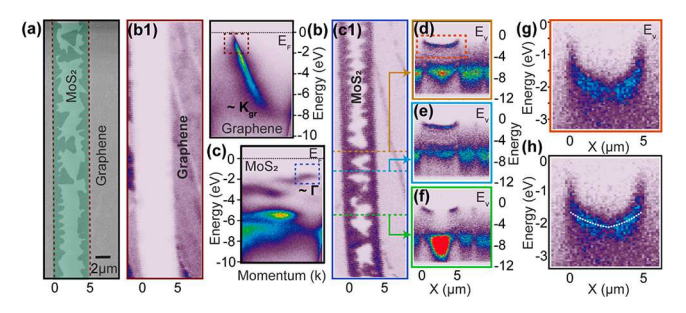


Figure 3. (a) False color scanning electron micrograph of an intentionally non-coalesced EG/MoS, lateral heterostructure. The MoS₂ nucleates from the edges of the EG and grows outwards. Hence, the darker triangular features are the MoS2 with the lighter region being the exposed SiC substrate. (b and c) Two E vs k ARPES band structure maps focusing specifically on EG and MoS₂, respectively. Panels (b1) and (c1) use the E vs k ARPES band structure maps shown in panels (b) and (c) to obtain the spatial distribution of EG and MoS2. Darker contrast corresponds to higher intensity. Upon overlaying panels (b1) and (c1), surface morphology similar to that in panel (a) is revealed. Because these measurements are made with separate instruments, we have found similar regions of the same sample but they are not exactly superimposable. Horizontal cuts at different y-values are taken for MoS₂ shown in panels (d-f). Panel (f) specifically focuses on an uncoalesced region to see the spatial variation of the bands. Panel (g) is a zoomed in version of panel (d) displaying an ~500 meV voltage drop from the EG/MoS2 interface to the center of the channel. (h) Band bending as predicted by first-principles calculations in white overlaid on the experimental nano ARPES results presented in panel (g). The agreement indicates that the grown interface is relatively clean, leading to a low amount of surface states and a considerable Schottky barrier.

junction to the center of the channel. Figure 3(b,c) shows two ARPES measured E vs k band structure maps. A darker contrast indicates a higher intensity (scale bars for each panel are shown in Supporting Information, section S.4). Figure 3(b) focuses on a sample region containing only graphene, showing the well-characterized π -band that crosses the Fermi level at K. Using the 4D dataset to extract the total intensity from the (E_t) k) region that highlights this π -band (dark red dashed rectangle in Figure 3b), and plotting the result as a function of (x, y), the spatial distribution of graphene across the scanned sample area is obtained as shown in Figure 3(b1). Similarly, focusing on a region containing only MoS₂ (Figure 3c), and integrating over (E, k) such as to only highlight MoS₂ valence band states (blue rectangle in Figure 3c), we can reveal the distribution of MoS2 across the sample as shown in Figure 3(c1). Upon overlaying, panels (b1) and (c1) of Figure 3 reproduce the surface morphology as obtained from a scanning electron micrograph on a similar channel in Figure 3(a). Because these measurements are made with separate instruments, we have found similar regions of the same sample but they are not exactly superimposable. The 5 μ m channel etched in the EG is filled with triangles of MoS2. An EG/MoS2 heterostructure synthesized in this manner has an overlap of the MoS₂ on the EG at the patterned edge for a length scale of ~200 nm, on the order of the nano-ARPES resolution, and consequently is thicker at the patterned edge.³³ The intentionally non-coalesced lateral heterostructure system exhibits regions where the MoS₂ bridges the channel, which serve to explore band bending within the channel. Step edges on the SiC substrate are readily observed as lines with lighter contrast in Figure 3(b1). Corresponding dark lines in Figure 3(c1)

show the favorable nucleation of MoS₂ at the step edges of EG, which are known to be thicker and more defective compared to the EG on the terraces.⁶⁷ To understand how the electronic band structure changes at the EG/MoS2 heterostructure interface, we focus on the MoS2 valence band maximum (VBM) and observe how it bends upon moving away from the interface. Horizontal cuts at select y-values, with differing MoS₂ coverage, are taken from Figure 3(c1), marked by the yellow, cyan, and green lines, allowing for E versus x plots (Figure 3d– f) mapping the variation of the MoS₂ VBM across the EG/ MoS₂/EG interface. Figure 3(g) is a close-up of Figure 3(d), where the variation of the VBM is seen along a cut (yellow line in Figure 3c1) where the channel is completely coalesced with MoS₂. Here, it is observed that the VBM bends strongly downwards, from approximately -1.5 eV at the interface to -2 eV near the channel center. The screening at this position is isotropic (Figure 3g), leading to symmetric band bending with respect to the center of the channel. The band bending in Figure 3(e) is similar in magnitude but highly asymmetric, possibly as a result of anisotropic screening due to variation in domain sizes and growth modes in both directions. Figure 3(f) shows the cut along the green line in Figure 3(c1), where the MoS₂ channel is not coalesced and the VBM is interrupted. The precise shape of the band bending is a function of the specific electrostatic environment, determined by coalescence in the channel as well as charge carrier screening from the EG and the SiC substrate. We assume a rigid band model and extrapolate the bending of the VBM observed via nano-ARPES to be the same as the bending of the conduction band minimum (CBM). The direction of band bending indicates that the electronic charges are transferred out from the MoS₂ into the EG upon formation of the heterostructure, indicating the MoS₂ donates electrons to the EG in order to attain equilibrium. This band bending is thus a direct observation of the Schottky barrier at the EG/MoS₂ lateral heterostructure interface.

Density functional theory calculations can help interpret the spatial distribution of the potential at the EG/MoS₂ heterostructure interface. Following the Schottky barrier calculations (Figure 2), the potential $\varphi(x)$ within the semiconductor can be expressed as⁶⁸

$$\varphi(x) = -\frac{e_0 N_{\rm d}}{2\varepsilon \varepsilon_0} x^2 - \frac{\mathrm{d}\varphi}{\mathrm{d}z} (z_{\rm c}) x + \phi_{\rm s} + \varphi_0 \tag{2}$$

where x is the distance from the EG/MoS₂ interface and φ_0 is a constant to fulfill the boundary condition at the midpoint of the leftmost edge of the band region in Figure 3(g). The expected band bending is plotted over the experimental results in Figure 3(h). Because the MoS₂ is symmetrically terminated on both sides with an EG junction, the band bending in Figure 3(h) is shown according to eq 2 until the midpoint of the MoS₂ region, and then the potential is symmetrically mirrored on the other side. In our calculations, with only \sim 2.5 μ m of space on each side for the potential to decrease, the dopant density is not high enough to reach the theoretically predicted height of the Schottky barrier, instead only forming a barrier of 0.38 eV. This leads to some uncertainty in whether the overall potential should be shifted slightly down to match the Fermi level of the EG, but the range of uncertainty nevertheless is small compared to the extent of the observed band regions. The agreement of the theoretical potential with its nano-ARPES counterpart at the carrier concentration of 4×10^{12}

cm⁻³ strongly indicates that the synthesized interface is atomically clean with a low density of defects. This work highlights the capabilities of first-principles methods to understand behaviors at semiconductor junctions and facilitate the interpretation of experiments, providing physical insights and predictive trends.

CONCLUSION

EG/MoS₂/EG symmetric heterostructure has >10× larger photocurrent at the EG/MoS₂ interfaces, as compared to metal/MoS₂/EG asymmetric heterostructure, with a uniform built-in field through the length of the symmetric heterostructure device. The electronic Schottky barrier at the EG/ MoS_2 interface is predicted to be $\sim 2 \times$ lower than that of Ti/ MoS_2 using DFT, corroborated by experimental I-V-Tmeasurements. To further understand the transfer of photogenerated charge at the EG/MoS₂ interface, spatial variations of electronic bands are investigated using nano-ARPES. The valence band maximum in MoS2 bends ~500 meV over a length scale of 2-3 μ m, matching theoretical calculations. This comprehensive understanding of the photophysics and optoelectronic properties of the EG/MoS₂ lateral heterostructure system can be extrapolated to other systems in order to build a library of photo-active heterostructure interfaces with properties tailored for specific optoelectronic applications. We have highlighted the utility of first-principles calculations to interpret the electrical response at heterostructure interfaces. The photocurrent measurements presented here are demonstrated to be a simple probe to measure the electronic uniformity of the synthesized lateral heterostructure interfaces. This simple probe-based technique can be adopted easily by the 2D materials' growth community in order to check for electronic uniformity at domain boundaries of synthesized 2D materials and heterostructures over large areas alongside morphological uniformity.

METHODS

Sample Preparation. The method of sample preparation is the same as in our previous publications. 33,69 EG is grown at 1800 °C in a three-phase, hot-zone, graphite furnace via silicon sublimation from the (0001) face of vanadium-doped semi-insulating 6H SiC. It is then patterned using standard ultraviolet photolithography, and a mixture of oxygen and argon (O₂/Ar) is used for a reactive ion etch to remove the EG outside of the patterns, leaving behind periodically spaced graphene rectangles of fixed length (5 μ m) that ultimately constitute the contacts to the MoS₂ channel. Powder vaporization in a horizontal quartz tube furnace is used to synthesize MoS $_2$ at 800 $^{\circ}$ C just outside the graphene rectangles, using 2-3 mg of molybdenum trioxide (MoO₃) powder and 200 mg of sulfur (S) as the precursors. Following the synthesis of EG/MoS₂ lateral heterostructure, an SF₆/ O₂ reactive ion etch is used to isolate the MoS₂ between the graphene electrodes. Contact regions are then lithographically patterned, briefly exposed to an O2 plasma, and Ti/Au (5/15 nm) metal is deposited via electron-beam evaporation, followed by lift off in PRS 3000 photoresist remover. Ti is evaporated onto the sample at a vacuum of $\sim 10^{-9}$ Torr in an electron beam evaporation chamber at a rate of \sim 0.5 Å/s up to a thickness of $\sim 5 \text{ nm}$. Au is then evaporated at the rate of \sim 1 Å/s upto a thickness of \sim 20 nm. The sample chuck is cooled to 0 °C during the entire deposition process.

Photocurrent Measurements. We measure the photocurrent by scanning a tunable Ar/Kr laser at 488 nm (2.54 eV) across the area of the investigated lateral heterojunctions with piezo stages. The laser is focused on the heterojunctions by a $100 \times$ Mitutoyo Plan Apo objective (f = 200 mm) to a diffraction limited spot size of $\sim 0.8 \ \mu \text{m}$ (FWHM). The resulting photocurrent at each point is measured by a

succession of a current preamplifier (Ithaco 1211) at a sensitivity of 10^{-7} A/V and a digital multimeter (Agilent 34401A). All measurements are performed in vacuum (10^{-6} mbar) at room temperature. The SiC substrate does not contribute to the photocurrent at the wavelength of the laser utilized.

Computational Details. We utilize the plane-wave density functional theory code QUANTUM-ESPRESSO.⁷⁰ We create 4 layer thick slabs of each material as shown in Figure 2, which was determined to be sufficient to converge the Fermi energy to 50 meV. We utilize Perdew-Burke-Ernzerhof (PBE) exchange-correlation functionals⁷¹ with norm-conserving Vanderbilt pseudopotentials from the PseudoDojo library for all the calculations in the main text.⁷² For comparison, in Table S.2.1, we also use PBEsol,⁷³ PZ,⁷⁴ and PW91⁷⁵ PAW pseudopotentials from the PSLibrary. 76 We sample the Brillioun zone with a 4 × 4 × 1 Monkhorst-Pack grid and 0.0001 Ry of Marzari-Vanderbilt smearing.⁷⁷ We select wavefunction and charge density kinetic energy cutoffs of 50 and 200 Ry, respectively. By aligning the potential of the vacuum region to zero, we can obtain the wavefunction of different slabs as the negative of the Fermi level (i.e. $\phi = -\epsilon_{\rm F}$). We follow the procedure outlined in the text to obtain the Schottky barrier of the material (see Supporting Information, section S2 for a summarized procedure). The slabs and interface were generated using the pymatgen utility.7

I–V–T Measurements. Electrostatic double-layer (EDL) gating is implemented in an Oxford Optistat closed-cycle helium-cooled pulse tube cryostat using (PEO) $_{76}$:CsClO $_4$ as the electrolyte with mobile ions, allowing the I–V–T measurements in the temperature range of 3–300 K. Biasing the EG/MoS $_2$ /EG and metal/MoS $_2$ /EG channel ($V_{\rm ds}$) and biasing the gate ($V_{\rm g}$) are both performed with a dual-channel Keysight B2912A Precision Source/Measure Unit. In order to arrest the mobile ions in the electrolyte dielectric at a certain gate voltage, the $V_{\rm g}$ is applied at room temperature, and then the system is cooled to 3 K. The temperature is slowly raised in steps of 5 K until 300 K, and the source—drain current ($I_{\rm ds}$) was measured at each temperature at a fixed $V_{\rm ds}$ of 100 mV. The $V_{\rm g}$ is then increased by 0.5 V, and the measurement cycle is repeated. A side gate geometry is implemented.

Nano-ARPES. Angle-resolved photoemission intensity maps were recorded using a focused synchrotron beam and a Scienta R4000 analyzer at the MAESTRO beamline of the Advanced Light Source. A Fresnel zone plate was used to focus the beam. The zone plate used in the experiments allows a minimum spot size of 120 nm. For ARPES, the photon energy was set to $E_{\rm ph}$ = 98 eV; the detector resolution was 125 meV; the entrance slit width and height were 50 μ m, and the sample was held at room temperature. From the nano-ARPES maps, we determined a spatial resolution of ~300 nm for the measurements presented. The base pressure during the measurements was below 10⁻¹¹ mbar. ARPES was conducted on the same samples as discussed in ref 69. The samples were synthesized ex situ (as detailed in ref 33), exposed to ambient conditions, and then transferred into the nano-ARPES chamber. Prior to the X-ray measurements, the samples were annealed at 100 $^{\circ}\text{C}$ under vacuum for 30 min to remove surface adsorbates.

ASSOCIATED CONTENT

Supporting Information

The Supporting Information is available free of charge at https://pubs.acs.org/doi/10.1021/acsnano.0c02527.

Additional acquired data, analysis, and measurement limitations explained in detail (PDF)

AUTHOR INFORMATION

Corresponding Author

Joshua A. Robinson – Department of Materials Science and Engineering, Center for 2-Dimensional and Layered Materials, 2-Dimensional Crystal Consortium, and Center for Atomically Thin Multifunctional Coatings, The Pennsylvania State University, University Park, Pennsylvania 16802, United States; Phone: 1 (814) 863-8567; Email: jrobinson@psu.edu

Authors

- Shruti Subramanian Department of Materials Science and Engineering and Center for 2-Dimensional and Layered Materials, The Pennsylvania State University, University Park, Pennsylvania 16802, United States; orcid.org/0000-0002-8933-9486
- Quinn T. Campbell Department of Materials Science and Engineering, The Pennsylvania State University, University Park, Pennsylvania 16802, United States; Center for Computing Research, Sandia National Laboratories, Albuquerque, New Mexico 87185, United States;
 orcid.org/0000-0003-1377-3769
- Simon K. Moser Advanced Light Source, E. O. Lawrence Berkeley National Laboratory,, Berkeley, California 94720, United States; Physikalisches Institut and Würzburg-Dresden Cluster of Excellence ct.qmat, Universität Würzburg, 97074 Würzburg, Germany
- Jonas Kiemle Walter Schottky Institut and Physik Department, Technische Universität München, 85748 Garching, Germany
- Philipp Zimmermann Walter Schottky Institut and Physik Department, Technische Universität München, 85748 Garching, Germany
- Paul Seifert Walter Schottky Institut and Physik
 Department, Technische Universität München, 85748
 Garching, Germany; ICFO Institut de Ciencies Fotoniques,
 The Barcelona Institute of Science and Technology,
 Castelldefels, Barcelona 08860, Spain; ◎ orcid.org/00000002-4781-7099
- Florian Sigger Walter Schottky Institut and Physik Department, Technische Universität München, 85748 Garching, Germany
- Deeksha Sharma Department of Mechanical Engineering, The Pennsylvania State University, University Park, Pennsylvania 16802, United States
- Hala Al-Sadeg Department of Materials Science and Engineering, The Pennsylvania State University, University Park, Pennsylvania 16802, United States
- Michael Labella, III Nanofabrication Facility, The Pennsylvania State University, University Park, Pennsylvania 16802, United States
- Dacen Waters Department of Physics, Carnegie Mellon University, Pittsburgh, Pennsylvania 15213, United States; orcid.org/0000-0003-3588-0039
- Randall M. Feenstra Department of Physics, Carnegie Mellon University, Pittsburgh, Pennsylvania 15213, United States; orcid.org/0000-0001-7120-5685
- Roland J. Koch Advanced Light Source, E. O. Lawrence Berkeley National Laboratory,, Berkeley, California 94720, United States; Oorcid.org/0000-0001-5748-8463
- Chris Jozwiak Advanced Light Source, E. O. Lawrence Berkeley National Laboratory,, Berkeley, California 94720, United States; Occid.org/0000-0002-0980-3753
- Aaron Bostwick Advanced Light Source, E. O. Lawrence Berkeley National Laboratory,, Berkeley, California 94720, United States
- Eli Rotenberg Advanced Light Source, E. O. Lawrence Berkeley National Laboratory,, Berkeley, California 94720, United States; o orcid.org/0000-0002-3979-8844

- Ismaila Dabo Department of Materials Science and Engineering, The Pennsylvania State University, University Park, Pennsylvania 16802, United States; orcid.org/0000-0003-0742-030X
- Alexander W. Holleitner Walter Schottky Institut and Physik Department, Technische Universität München, 85748 Garching, Germany; oorcid.org/0000-0002-8314-4397
- Thomas E. Beechem Center for Integrated Nanotechnologies, Sandia National Laboratories, Albuquerque, New Mexico 87185, United States
- Ursula Wurstbauer Walter Schottky Institut and Physik Department, Technische Universität München, 85748 Garching, Germany; Institute of Physics, University of Munster, 48149 Münster, Germany

Complete contact information is available at: https://pubs.acs.org/10.1021/acsnano.0c02527

Notes

The authors declare no competing financial interest.

ACKNOWLEDGMENTS

S.S. and J.A.R. acknowledge funding from NSF CAREER (Award: 1453924). S.K.M. acknowledges support by the Swiss National Science Foundation (Grant No. P300P2-171221). This research used resources of the Advanced Light Source, which is a DOE Office of Science User Facility under Contract No. DE-AC02-05CH11231. P.S. acknowledges financial support from the Alexander von Humboldt foundation and the German federal ministry of education and research within the Feodor Lynen program. D.S. acknowledges funding from the National Science Foundation via Award Number EFMA 1433378 and EFMA 1433307. H.A.-S. was supported by the EXPEC Advanced Research Center, Petroleum Engineering and Development Department at Saudi Aramco. D.W. and R.M.F.'s contribution was supported in part by the Center for Low Energy Systems Technology (LEAST), one of six centers of STARnet, a Semiconductor Research Corporation program sponsored by MARCO and DARPA. I.D. acknowledges financial support from the National Science Foundation under Grant No. DMREF-1729338. U.W. was funded by the Deutsche Forschungsgemeinschaft (DFG, German Research Foundation) under Germany's Excellence Strategy - EXC 2089/1-390776260. This work was performed, in part, at the Center for Integrated Nanotechnologies, an Office of Science User Facility operated for the U.S. Department of Energy (DOE) Office of Science. Sandia National Laboratories is a multimission laboratory managed and operated by National Technology & Engineering Solutions of Sandia, LLC, a wholly owned subsidiary of Honeywell International, Inc., for the U.S. DOE's National Nuclear Security Administration under contract DE-NA-0003525. The views expressed in the article do not necessarily represent the views of the U.S. DOE or the United States Government.

REFERENCES

- (1) Liu, X.; Galfsky, T.; Sun, Z.; Xia, F.; Lin, E.; Lee, Y.-H.; Kéna-Cohen, S.; Menon, V. M. Strong Light—Matter Coupling in Two-Dimensional Atomic Crystals. *Nat. Photonics* **2015**, *9*, 30–34.
- (2) Wu, S.; Buckley, S.; Jones, A. M.; Ross, J. S.; Ghimire, N. J.; Yan, J.; Mandrus, D. G.; Yao, W.; Hatami, F.; Vučković, J.; Majumdar, A.; Xu, X. Control of Two-Dimensional Excitonic Light Emission *via* Photonic Crystal. 2D *Mater.* **2014**, *1*, No. 011001.

- (3) Das, S.; Gulotty, R.; Sumant, A. V.; Roelofs, A. All Two-Dimensional, Flexible, Transparent, and Thinnest Thin Film Transistor. *Nano Lett.* **2014**, *14*, 2861–2866.
- (4) Kim, S. J.; Choi, K.; Lee, B.; Kim, Y.; Hong, B. H. Materials for Flexible, Stretchable Electronics: Graphene and 2D Materials. *Annu. Rev. Mater. Res.* **2015**, *45*, 63–84.
- (5) Briggs, N.; Subramanian, S.; Lin, Z.; Li, X.; Zhang, X.; Zhang, K.; Xiao, K.; Geohegan, D.; Wallace, R.; Chen, L.-Q.; Terrones, M.; Ebrahimi, A.; Das, S.; Redwing, J.; Hinkle, C.; Momeni, K.; van Duin, A.; Crespi, V.; Kar, S.; Robinson, J. A. A Roadmap for Electronic Grade 2D Materials. 2D Mater. 2019, 6, No. 022001.
- (6) Zhang, W.; Wang, Q.; Chen, Y.; Wang, Z.; Wee, A. T. S. van der Waals Stacked 2D Layered Materials for Optoelectronics. 2D Mater. 2016, 3, No. 022001.
- (7) Wang, Q. H.; Kalantar-Zadeh, K.; Kis, A.; Coleman, J. N.; Strano, M. S. Electronics and Optoelectronics of Two-Dimensional Transition Metal Dichalcogenides. *Nat. Nanotechnol.* **2012**, *7*, 699–712
- (8) Mak, K. F.; Shan, J. Photonics and Optoelectronics of 2D Semiconductor Transition Metal Dichalcogenides. *Nat. Photonics* **2016**, *10*, 216–226.
- (9) Parzinger, E.; Hetzl, M.; Wurstbauer, U.; Holleitner, A. W. Contact Morphology and Revisited Photocurrent Dynamics in Monolayer MoS₂. npj 2D Mater. Appl. **2017**, 1, 40.
- (10) Mak, K. F.; McGill, K. L.; Park, J.; McEuen, P. L. Valleytronics. The Valley Hall Effect in MoS₂ Transistors. *Science* **2014**, 344, 1489–1492.
- (11) Deng, D.; Novoselov, K. S.; Fu, Q.; Zheng, N.; Tian, Z.; Bao, X. Catalysis with Two-Dimensional Materials and Their Heterostructures. *Nat. Nanotechnol.* **2016**, *11*, 218–230.
- (12) Li, H.; Xiao, J.; Fu, Q.; Bao, X. Confined Catalysis under Two-Dimensional Materials. *Proc. Natl. Acad. Sci. U. S. A.* **2017**, *114*, 5930–5934.
- (13) Machado, B. F.; Serp, P. Graphene-Based Materials for Catalysis. *Catal. Sci. Technol.* **2012**, *2*, 54–75.
- (14) Chimene, D.; Alge, D. L.; Gaharwar, A. K. Two-Dimensional Nanomaterials for Biomedical Applications: Emerging Trends and Future Prospects. *Adv. Mater.* **2015**, 27, 7261–7284.
- (15) Kurapati, R.; Kostarelos, K.; Prato, M.; Bianco, A. Biomedical Uses for 2D Materials Beyond Graphene: Current Advances and Challenges Ahead. *Adv. Mater.* **2016**, *28*, 6052–6074.
- (16) Lee, H. U.; Park, S. Y.; Lee, S. C.; Choi, S.; Seo, S.; Kim, H.; Won, J.; Choi, K.; Kang, K. S.; Park, H. G.; Kim, H.-S.; An, H. R.; Jeong, K.-H.; Lee, Y.-C.; Lee, J. Black Phosphorus (BP) Nanodots for Potential Biomedical Applications. *Small* **2016**, *12*, 214–219.
- (17) Ebrahimi, A.; Zhang, K.; Dong, C.; Subramanian, S.; Butler, D.; Bolotsky, A.; Goodnight, L.; Cheng, Y.; Robinson, J. A. FeS_x: Graphene Heterostructures: Nanofabrication-Compatible Catalysts for Ultra-Sensitive Electrochemical Detection of Hydrogen Peroxide. Sens. Actuators, B **2019**, 285, 631–638.
- (18) Kannan, P. K.; Late, D. J.; Morgan, H.; Rout, C. S. Recent Developments in 2D Layered Inorganic Nanomaterials for Sensing. *Nanoscale* **2015**, *7*, 13293–13312.
- (19) Li, X.; Zhang, F.; Niu, Q. Unconventional Quantum Hall Effect and Tunable Spin Hall Effect in Dirac Materials: Application to an Isolated MoS₂ Trilayer. *Phys. Rev. Lett.* **2013**, *110*, No. 066803.
- (20) Wang, X.; Sun, G.; Li, N.; Chen, P. Quantum Dots Derived from Two-Dimensional Materials and Their Applications for Catalysis and Energy. *Chem. Soc. Rev.* **2016**, *45*, 2239–2262.
- (21) Saha, S. K.; Baskey, M.; Majumdar, D. Graphene Quantum Sheets: A New Material for Spintronic Applications. *Adv. Mater.* **2010**, 22, 5531–5536.
- (22) Ananthanarayanan, A.; Wang, X.; Routh, P.; Sana, B.; Lim, S.; Kim, D.-H.; Lim, K.-H.; Li, J.; Chen, P. Facile Synthesis of Graphene Quantum Dots from 3D Graphene and Their Application for Fe³⁺ Sensing. *Adv. Funct. Mater.* **2014**, *24*, 3021–3026.
- (23) Zhang, Z.; Zhang, J.; Chen, N.; Qu, L. Graphene Quantum Dots: An Emerging Material for Energy-Related Applications and Beyond. *Energy Environ. Sci.* **2012**, *5*, 8869.

- (24) Costanzo, D.; Jo, S.; Berger, H.; Morpurgo, A. F. Gate-Induced Superconductivity in Atomically Thin MoS₂ Crystals. *Nat. Nanotechnol.* **2016**, *11*, 339–344.
- (25) Miller, B.; Lindlau, J.; Bommert, M.; Neumann, A.; Yamaguchi, H.; Holleitner, A.; Högele, A.; Wurstbauer, U. Tuning the Fröhlich Exciton-Phonon Scattering in Monolayer MoS₂. *Nat. Commun.* **2019**, *10*. 807.
- (26) Branny, A.; Kumar, S.; Proux, R.; Gerardot, B. D. Deterministic Strain-Induced Arrays of Quantum Emitters in a Two-Dimensional Semiconductor. *Nat. Commun.* **2017**, *8*, 15053.
- (27) Kumar, S.; Kaczmarczyk, A.; Gerardot, B. D. Strain-Induced Spatial and Spectral Isolation of Quantum Emitters in Mono- and Bilayer WSe₂. *Nano Lett.* **2015**, *15*, *7567–7573*.
- (28) Klein, J.; Lorke, M.; Florian, M.; Sigger, F.; Sigl, L.; Rey, S.; Wierzbowski, J.; Cerne, J.; Müller, K.; Mitterreiter, E.; Zimmermann, P.; Taniguchi, T.; Watanabe, K.; Wurstbauer, U.; Kaniber, M.; Knap, M.; Schmidt, R.; Finley, J. J.; Holleitner, A. W. Site-Selectively Generated Photon Emitters in Monolayer MoS₂ via Local Helium Ion Irradiation. Nat. Commun. 2019, 10, 2755.
- (29) Di Bartolomeo, A.; Pelella, A.; Liu, X.; Miao, F.; Passacantando, M.; Giubileo, F.; Grillo, A.; Iemmo, L.; Urban, F.; Liang, S. Pressure-Tunable Ambipolar Conduction and Hysteresis in Thin Palladium Diselenide Field Effect Transistors. *Adv. Funct. Mater.* **2019**, 29, 1902483.
- (30) Chernikov, A.; Berkelbach, T. C.; Hill, H. M.; Rigosi, A.; Li, Y.; Aslan, O. B.; Reichman, D. R.; Hybertsen, M. S.; Heinz, T. F. Exciton Binding Energy and Nonhydrogenic Rydberg Series in Monolayer WS₂. *Phys. Rev. Lett.* **2014**, *113*, No. 076802.
- (31) Wang, Z.; Rhodes, D. A.; Watanabe, K.; Taniguchi, T.; Hone, J. C.; Shan, J.; Mak, K. F. Evidence of High-Temperature Exciton Condensation in Two-Dimensional Atomic Double Layers. *Nature* **2019**, *574*, 76–80.
- (32) Wu, F.; Lovorn, T.; MacDonald, A. H. Topological Exciton Bands in Moiré Heterojunctions. *Phys. Rev. Lett.* **2017**, *118*, 147401.
- (33) Subramanian, S.; Deng, D. D.; Xu, K.; Simonson, N.; Wang, K.; Zhang, K.; Li, J.; Feenstra, R.; Fullerton-Shirey, S. K.; Robinson, J. A. Properties of Synthetic Epitaxial Graphene/Molybdenum Disulfide Lateral Heterostructures. *Carbon* 2017, 125, 551–556.
- (34) Jin, Y.; Joo, M.-K.; Moon, B. H.; Kim, H.; Lee, S.; Jeong, H. Y.; Kwak, H. Y.; Lee, Y. H. Coulomb Drag Transistor *via* Graphene/MoS₂ Heterostructures. 2017, 1710.11365. ArXiV. http://arxiv.org/abs/1710.11365 (accessed 2020-06-24).
- (35) Novoselov, K. S.; Geim, A. K.; Morozov, S. V.; Jiang, D.; Katsnelson, M. I.; Grigorieva, I. V.; Dubonos, S. V.; Firsov, A. A. Two-Dimensional Gas of Massless Dirac Fermions in Graphene. *Nature* **2005**, 438, 197–200.
- (36) Lopez-Sanchez, O.; Lembke, D.; Kayci, M.; Radenovic, A.; Kis, A. Ultrasensitive Photodetectors Based on Monolayer MoS₂. *Nat. Nanotechnol.* **2013**, *8*, 497–501.
- (37) Sulas-Kern, D. B.; Zhang, H.; Li, Z.; Blackburn, J. L. Microsecond Charge Separation at Heterojunctions between Transition Metal Dichalcogenide Monolayers and Single-Walled Carbon Nanotubes. *Mater. Horiz.* **2019**, *6*, 2103–2111.
- (38) Park, S.; Mutz, N.; Schultz, T.; Blumstengel, S.; Han, A.; Aljarb, A.; Li, L.-J.; List-Kratochvil, E. J W; Amsalem, P.; Koch, N. Direct Determination of Monolayer MoS₂ and WSe₂ Exciton Binding Energies on Insulating and Metallic Substrates. 2D Mater. 2018, 5, No. 025003.
- (39) Latini, S.; Winther, K. T.; Olsen, T.; Thygesen, K. S. Interlayer Excitons and Band Alignment in $MoS_2/HBN/WSe_2$ van der Waals Heterostructures. *Nano Lett.* **2017**, *17*, 938–945.
- (40) Thilagam, A. Exciton Complexes in Low Dimensional Transition Metal Dichalcogenides. J. Appl. Phys. 2014, 116, No. 053523.
- (41) Di Bartolomeo, A.; Genovese, L.; Foller, T.; Giubileo, F.; Luongo, G.; Croin, L.; Liang, S.-J.; Ang, L. K.; Schleberger, M. Electrical Transport and Persistent Photoconductivity in Monolayer MoS2 Phototransistors. *Nanotechnology* **2017**, *28*, 214002.

- (42) Fortin, E.; Sears, W. M. Photovoltaic Effect and Optical Absorption in MoS₂. *J. Phys. Chem. Solids* **1982**, *43*, 881–884.
- (43) Hong, T.; Chamlagain, B.; Hu, S.; Weiss, S. M.; Zhou, Z.; Xu, Y.-Q. Plasmonic Hot Electron Induced Photocurrent Response at MoS,—Metal Junctions. *ACS Nano* **2015**, *9*, 5357–5363.
- (44) Gross, R.; Marx, A.; Einzel, D.; Geprägs, S. Festkörperphysik : Aufgaben Und Lösungen; De Gruyter: Berlin, Germany, 2018.
- (45) Sun, D.; Aivazian, G.; Jones, A. M.; Ross, J. S.; Yao, W.; Cobden, D.; Xu, X. Ultrafast Hot-Carrier-Dominated Photocurrent in Graphene. *Nat. Nanotechnol.* **2012**, *7*, 114–118.
- (46) Woessner, A.; Alonso-González, P.; Lundeberg, M. B.; Gao, Y.; Barrios-Vargas, J. E.; Navickaite, G.; Ma, Q.; Janner, D.; Watanabe, K.; Cummings, A. W.; Taniguchi, T.; Pruneri, V.; Roche, S.; Jarillo-Herrero, P.; Hone, J.; Hillenbrand, R.; Koppens, F. H. L. Near-Field Photocurrent Nanoscopy on Bare and Encapsulated Graphene. *Nat. Commun.* 2016, 7, 10783.
- (47) Zhang, W.; Chuu, C.-P.; Huang, J.-K.; Chen, C.-H.; Tsai, M.-L.; Chang, Y.-H.; Liang, C.-T.; Chen, Y.-Z.; Chueh, Y.-L.; He, J.-H.; Chou, M.-Y.; Li, L.-J. Ultrahigh-Gain Photodetectors Based on Atomically Thin Graphene-MoS₂ Heterostructures. *Sci. Rep.* **2015**, *4*, 3826
- (48) Prechtel, L.; Song, L.; Schuh, D.; Ajayan, P.; Wegscheider, W.; Holleitner, A. W. Time-Resolved Ultrafast Photocurrents and Terahertz Generation in Freely Suspended Graphene. *Nat. Commun.* **2012**, *3*, 646.
- (49) De Arco, L. G.; Zhang, Y.; Kumar, A.; Zhou, C. Synthesis, Transfer, and Devices of Single- and Few-Layer Graphene by Chemical Vapor Deposition. *IEEE Trans. Nanotechnol.* **2009**, *8*, 135–138.
- (50) Heydrich, S.; Hirmer, M.; Preis, C.; Korn, T.; Eroms, J.; Weiss, D.; Schüller, C. Scanning Raman Spectroscopy of Graphene Antidot Lattices: Evidence for Systematic *p*-Type Doping. *Appl. Phys. Lett.* **2010**, *97*, No. 043113.
- (51) Spectral Reflectance Calculator for Thin-Film Stacks. https://www.filmetrics.com/reflectance-calculator (accessed 2020-06-24).
- (52) Heavens, O. S.; Singer, S. F. Optical Properties of Thin Solid Films. *Phys. Today* **1956**, *9*, 24–26.
- (53) Azzam, R. M. A.; Bashara, N. M.; Ballard, S. S. Ellipsometry and Polarized Light. *Phys. Today* **1978**, *31*, 72–72.
- (54) Petrova-Mayor, A.; Gimbal, S. Advanced Lab on Fresnel Equations. Am. J. Phys. 2015, 83, 935-941.
- (55) Byrnes, S. J. Multilayer Optical Calculations; 2019, 1603.02720v4. ArXiv. https://arxiv.org/abs/1603.02720. (accessed 2020-06-24).
- (56) Lee, S. Y.; Kim, U. J.; Chung, J.; Nam, H.; Jeong, H. Y.; Han, G. H.; Kim, H.; Oh, H. M.; Lee, H.; Kim, H.; Roh, Y.-G.; Kim, J.; Hwang, S. W.; Park, Y.; Lee, Y. H. Large Work Function Modulation of Monolayer MoS₂ by Ambient Gases. *ACS Nano* **2016**, *10*, 6100–6107
- (57) Ziegler, D.; Gava, P.; Güttinger, J.; Molitor, F.; Wirtz, L.; Lazzeri, M.; Saitta, A. M.; Stemmer, A.; Mauri, F.; Stampfer, C. Variations in the Work Function of Doped Single- and Few-Layer Graphene Assessed by Kelvin Probe Force Microscopy and Density Functional Theory. *Phys. Rev. B: Condens. Matter Mater. Phys.* **2011**, 83, 235434.
- (58) Singh-Miller, N. E.; Marzari, N. Surface Energies, Work Functions, and Surface Relaxations of Low-Index Metallic Surfaces from First Principles. *Phys. Rev. B: Condens. Matter Mater. Phys.* **2009**, 80, 235407.
- (59) Giovannetti, G.; Khomyakov, P. A.; Brocks, G.; Karpan, V. M.; van den Brink, J.; Kelly, P. J. Doping Graphene with Metal Contacts. *Phys. Rev. Lett.* **2008**, *101*, No. 026803.
- (60) Campbell, Q.; Dabo, I. Quantum-Continuum Calculation of the Surface States and Electrical Response of Silicon in Solution. *Phys. Rev. B: Condens. Matter Mater. Phys.* **2017**, *95*, 205308.
- (61) Campbell, Q.; Fisher, D.; Dabo, I. Voltage-Dependent Reconstruction of Layered Bi₂WO₆ and Bi₂MoO₆ Photocatalysts and Its Influence on Charge Separation for Water Splitting. *Phys. Rev. Mater.* **2019**, *3*, No. 015404.

- (62) Santos, E. J. G.; Kaxiras, E. Electrically Driven Tuning of the Dielectric Constant in MoS₂ Layers. ACS Nano 2013, 7, 10741–10746.
- (63) Kim, S.; Konar, A.; Hwang, W.-S.; Lee, J. H.; Lee, J.; Yang, J.; Jung, C.; Kim, H.; Yoo, J.-B.; Choi, J.-Y.; Jin, Y. W.; Lee, S. Y.; Jena, D.; Choi, W.; Kim, K. High-Mobility and Low-Power Thin-Film Transistors Based on Multilayer MoS₂ Crystals. *Nat. Commun.* **2012**, 3, 1011.
- (64) Yu, L.; Lee, Y.-H.; Ling, X.; Santos, E. J. G.; Shin, Y. C.; Lin, Y.; Dubey, M.; Kaxiras, E.; Kong, J.; Wang, H.; Palacios, T. Graphene/MoS₂ Hybrid Technology for Large-Scale Two-Dimensional Electronics. *Nano Lett.* **2014**, *14*, 3055–3063.
- (65) Jin, C.; Rasmussen, F. A.; Thygesen, K. S. Tuning the Schottky Barrier at the Graphene/MoS₂ Interface by Electron Doping: Density Functional Theory and Many-Body Calculations. *J. Phys. Chem. C* **2015**, *119*, 19928–19933.
- (66) English, C. D.; Shine, G.; Dorgan, V. E.; Saraswat, K. C.; Pop, E. Improved Contacts to MoS₂ Transistors by Ultra-High Vacuum Metal Deposition. *Nano Lett.* **2016**, *16*, 3824–3830.
- (67) Riedl, C.; Coletti, C.; Starke, U. Structural and Electronic Properties of Epitaxial Graphene on SiC(0001): A Review of Growth, Characterization, Transfer Doping and Hydrogen Intercalation. *J. Phys. D: Appl. Phys.* **2010**, *43*, 374009.
- (68) Schmickler, W.; Santos, E. Interfacial Electrochemistry; Springer: Berlin, 2010.
- (69) Subramanian, S.; Xu, K.; Wang, Y.; Moser, S.; Simonson, N. A.; Deng, D.; Crespi, V. H.; Fullerton-Shirey, S. K.; Robinson, J. A. Tuning Transport across MoS₂/Graphene Interfaces *via* As-Grown Lateral Heterostructures. *npj* 2D Mater. Appl. **2020**, 4, 9.
- (70) Giannozzi, P.; Baroni, S.; Bonini, N.; Calandra, M.; Car, R.; Cavazzoni, C.; Ceresoli, D.; Chiarotti, G. L.; Cococcioni, M.; Dabo, I.; Dal Corso, A.; de Gironcoli, S.; Fabris, S.; Fratesi, G.; Gebauer, R.; Gerstmann, U.; Gougoussis, C.; Kokalj, A.; Lazzeri, M.; Martin-Samos, L.; et al. QUANTUM ESPRESSO: A Modular and Open-Source Software Project for Quantum Simulations of Materials. *J. Phys.: Condens. Matter* 2009, 21, 395502.
- (71) Perdew, J. P.; Burke, K.; Ernzerhof, M. Generalized Gradient Approximation Made Simple. *Phys. Rev. Lett.* **1996**, *77*, 3865–3868.
- (72) van Setten, M. J.; Giantomassi, M.; Bousquet, E.; Verstraete, M. J.; Hamann, D. R.; Gonze, X.; Rignanese, G.-M.; van Setten, M. J.; Giantomassi, M.; Bousquet, E.; Verstraete, M. J.; Hamann, D. R.; Gonze, X.; Rignanese, G.-M. The PseudoDojo: Training and Grading a 85 Element Optimized Norm-Conserving Pseudopotential Table. Comput. Phys. Commun. 2018, 226, 39–54.
- (73) Perdew, J. P.; Ruzsinszky, A.; Csonka, G. I.; Vydrov, O. A.; Scuseria, G. E.; Constantin, L. A.; Zhou, X.; Burke, K. Restoring the Density-Gradient Expansion for Exchange in Solids and Surfaces. *Phys. Rev. Lett.* **2008**, *100*, 136406.
- (74) Perdew, J. P.; Zunger, A. Self-Interaction Correction to Density-Functional Approximations for Many-Electron Systems. *Phys. Rev. B: Condens. Matter Mater. Phys.* **1981**, 23, 5048–5079.
- (75) Perdew, J. P.; Wang, Y. Accurate and Simple Analytic Representation of the Electron-Gas Correlation Energy. *Phys. Rev. B: Condens. Matter Mater. Phys.* **1992**, *45*, 13244–13249.
- (76) Dal Corso, A. Pseudopotentials Periodic Table: From H to Pu. Comput. Mater. Sci. 2014, 95, 337–350.
- (77) Marzari, N.; Vanderbilt, D.; Payne, M. C. Ensemble Density-Functional Theory for *ab Initio* Molecular Dynamics of Metals and Finite-Temperature Insulators. *Phys. Rev. Lett.* **1997**, 79, 1337–1340.
- (78) Ong, S. P.; Richards, W. D.; Jain, A.; Hautier, G.; Kocher, M.; Cholia, S.; Gunter, D.; Chevrier, V. L.; Persson, K. A.; Ceder, G. Python Materials Genomics (Pymatgen): A Robust, Open-Source Python Library for Materials Analysis. *Comput. Mater. Sci.* **2013**, *68*, 314–319.